

# Resorbable Dicalcium Phosphate Bone Substitutes Prepared by 3D Powder Printing

By Uwe Gbureck,\* Tanja Hölzel, Uwe Klammert, Kristian Würzler, Frank A. Müller, and Jake E. Barralet

Bioceramic bone substitutes with programmed architecture were manufactured at room temperature in this study using a novel 3D printing process that combined 3D powder printing with calcium phosphate cement chemistry. During printing, biphasic  $\alpha/\beta$ -tricalcium phosphate ( $\text{Ca}_3(\text{PO}_4)_2$ , TCP) powder reacted with a liquid component consisting of phosphoric acid solution to form a matrix of dicalcium phosphate dihydrate ( $\text{CaHPO}_4 \cdot \text{H}_2\text{O}$ , DCPD, brushite) and unreacted TCP. Printed samples showed compressive strengths between 0.9–8.7 MPa after printing depending on the acid concentration. A further strength improvement to a maximum of 22 MPa could be obtained by additional hardening of the samples in phosphoric acid for three one minute washes. After this treatment, the samples mainly consisted of brushite with minor phases of unreacted TCP and a lesser amount of dicalcium phosphate anhydrate ( $\text{CaHPO}_4$ , DCPA, monetite). Hydrothermal conversion of brushite to DCPA resulted in an increase of porosity of approximately 13 % and a decrease of strength to 15 MPa, however the resorption rate *in vivo* was increased as demonstrated after intramuscular implantation over 56 weeks. Major advantages compared with commonly used sintering techniques are the low processing temperature, which enables the fabrication of thermally instable and degradable matrices of secondary calcium phosphates.

## 1. Introduction

The replacement of bone, necessitated by trauma, disease or congenital deformity requires the use of grafts to fill space and to prevent fibrous tissue ingrowth during healing and to act as an osteoconductive scaffold for new bone formation. Synthetic bone replacement materials offer the advantages of having well-defined architecture and reproducibility compared with autologous bone grafts. Clinically favoured synthetic materials for bone defect repair are mainly based on calcium phosphate chemistry due to their chemical similarity to the mineral phase of bone<sup>[1,2]</sup> and are mainly provided as sintered blocks, powders and granules of tricalcium phosphate (TCP,  $\text{Ca}_3(\text{PO}_4)_2$ )<sup>[3]</sup> or of

hydroxyapatite (HA,  $\text{Ca}_{10}(\text{PO}_4)_6(\text{OH})_2$ ) as well as self setting calcium phosphate cements (CPC)<sup>[4,5]</sup> which harden *in situ* to form nanocrystalline hydroxyapatite or brushite after mixing with an aqueous phase depending on pH. Currently no material class can fulfil all clinical demands. Sintered hydroxyapatite bioceramic blocks are non-resorbable due to their insolubility caused in part by their microscale grain structure and are difficult to adapt to irregular defect structures.<sup>[6]</sup> TCP based materials are slowly soluble at physiological conditions and if applied in granule form, they can be moulded into defects. However, only defects which are surrounded by intact bone areas can be filled with granules. In contrast, CPC can be freely moulded and provide mechanical support of the surrounding soft tissue after setting. However it is clinically complicated to reconstruct complex bone structures (e.g., in the orbita or maxillary region) and the lack of macroporosity of CPC limits the repair use of large defect volumes. These problems could be overcome by using custom-made calcium phosphate implants with a defined architecture exactly fitting a patient specific defect. Various authors have described rapid prototyping techniques to fabricate hydroxyapatite scaffolds for bone repair or tissue engineering using selective laser sintering (SLS) or powder printing with an organic binder<sup>[7–14]</sup> to form green bodies prior to sintering. However, the high temperature applied during these processes always leads to microcrystalline implants and prevents the fabrication of components from hydrated compounds (e.g., brushite or octacalcium phosphate). Low temperature rapid prototyping of calcium phosphate implants is currently limited to indirect procedures using negative wax patterns for cement infiltration<sup>[15]</sup> or individual moulds for hot-pressing and gas-foaming of polylactid acid/amorphous calcium phosphate/calcite composites.<sup>[16]</sup>

[\*] Dr. U. Gbureck, T. Hölzel  
Department for Functional Materials in Medicine and Dentistry  
University of Würzburg  
Pleicherwall 2, 97070 Würzburg (Germany)  
E-mail: uwe.gbureck@fmz.uni-wuerzburg.de  
Dr. Dr. U. Klammert, Dr. Dr. K. Würzler  
Department of Cranio-Maxillo-Facial Surgery  
University of Würzburg  
Pleicherwall 2, 97070 Würzburg (Germany)  
Dr. F.A. Müller  
Department for Materials Science III – Biomaterials  
University of Erlangen-Nürnberg  
Henkestr. 91, 91052 Erlangen (Germany)  
Dr. J. E. Barralet  
Faculty of Dentistry  
McGill University  
Strathcona Anatomy & Dentistry Building  
3640 University St., Montreal, Quebec H3A 2B2 (Canada)

In this work we describe the processing of programmed implant structures via a calcium phosphate cement setting reaction during 3D powder printing such that calcium phosphate samples with a well defined architecture could be produced at room temperature. This study aimed to investigate the mechanical performance, dimensional accuracy and phase composition of the printed dicalcium phosphate dihydrate (brushite) structures. Brushite components were converted to monetite by hydrothermal reaction and degradation of monetite and brushite implants was compared *in vivo*.

## 2. Results

Printing TCP powder beds with dilute phosphoric acid (5–30 wt %,  $0.51\text{--}3.06\text{ mol l}^{-1}$ ) enabled the manufacturing of complex 3D structures as displayed in Figure 1. The compressive strength and the printing accuracy, determined according to the minimum and maximum radius and the height of the printed samples, dependent on the  $\text{H}_3\text{PO}_4$  concentration of the printing liquid is given in Table 1. Using a 5 % phosphoric acid solution resulted in a compressive strength of 0.9 MPa after



Figure 1. Examples of powder printed brushite samples.

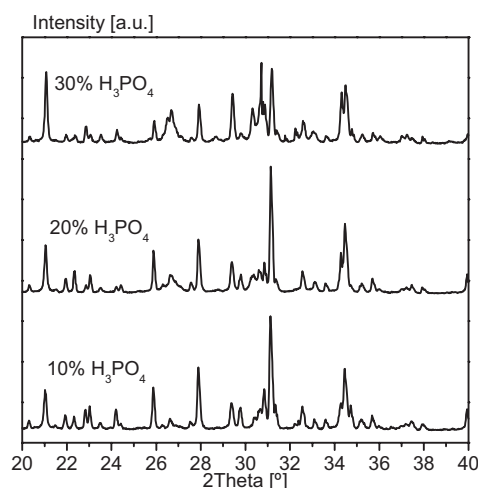


**Table 1.** Mean  $\pm$  standard deviation compressive strength, dimensions, and apparent density of samples printed with different  $\text{H}_3\text{PO}_4$  concentrations ( $n = 10$ ); theoretical dimensions of printed cylinders were  $h = 20.00\text{ mm}$  and  $r = 5.00\text{ mm}$ .

$\text{H}_3\text{PO}_4$ concentration [wt%]	Compressive strength [MPa]	Dimensions		
		$h$ [mm]	$r_{\min}$ [mm]	$r_{\max}$ [mm]
5	$0.9 \pm 0.1$	$20.4 \pm 0.1$	$4.9 \pm 0.0$	$5.1 \pm 0.1$
10	$3.0 \pm 0.3$	$20.8 \pm 0.1$	$5.0 \pm 0.0$	$5.2 \pm 0.0$
20	$5.3 \pm 0.6$	$20.8 \pm 0.1$	$5.1 \pm 0.0$	$5.2 \pm 0.0$
30	$8.7 \pm 1.3$	$20.7 \pm 0.1$	$5.1 \pm 0.0$	$5.3 \pm 0.1$

printing. However, higher concentration up to 30 % improved the strength to 8.7 MPa. Higher acid concentrations were found to be unsuitable for printing, probably due to the high viscosity of these solutions which prevented an accurate spraying of the acid solution from the print-head.

X-ray diffraction patterns of printed samples are shown in Figure 2. Detectable crystalline phases were in all cases unreacted TCP as well as brushite and a small amount of monetite. Rietveld refinement analysis of the diffraction patterns (Fig. 2) confirmed that during printing the amount of brushite increased with increasing acid concentration from 14 to 34 %. All samples contained a small proportion of monetite (approximately 4–14 %), which is thought to be a result of the strong acidic environment during printing as it was also observed for brushite cements composed of  $\beta$ -TCP and phosphoric acid.<sup>[17]</sup> Increasing the phosphoric acid concentration also increased the apparent density and hence decreased the porosity of samples from 50 % (10 %  $\text{H}_3\text{PO}_4$ ) to 41 % (30 %  $\text{H}_3\text{PO}_4$ ) as indicated in Table 2.

A further strength improvement of printed samples was obtained after repeated post hardening in diluted ( $2.04\text{ mol l}^{-1}$ ) phosphoric acid. Short immersion periods of 60s followed by rinsing the samples with water had to be used since a prolonged immersion in phosphoric acid caused considerable dissolution.

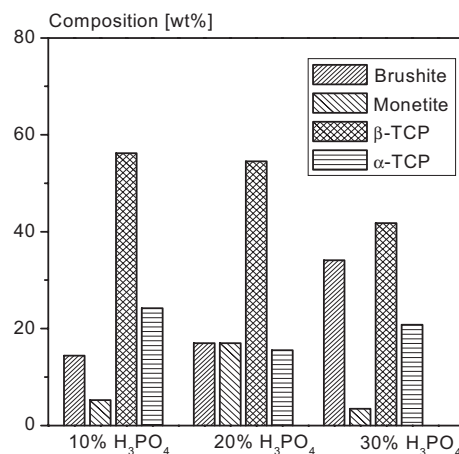


Figure 2. X-ray diffraction patterns of samples printed with different  $\text{H}_3\text{PO}_4$  concentrations (left) and quantitative phase composition according to Rietveld refinement analysis (right).

**Table 2.** Apparent density and porosity of powder printed samples.

H <sub>3</sub> PO <sub>4</sub> concentration [%]	Apparent density [g cm <sup>-3</sup> ]	Porosity [%]
5	1.37 ± 0.02	53
10	1.44 ± 0.01	50
20	1.53 ± 0.01	47
30	1.63 ± 0.04	41

The influence of this process on mechanical performance is displayed in Table 3. Repeated immersion in H<sub>3</sub>PO<sub>4</sub> resulted in a fourfold increase of the compressive strength of samples printed with 20 % H<sub>3</sub>PO<sub>4</sub> from 5.3 MPa to more than 22 MPa.

**Table 3.** Mean ± s.d. of compressive strength (CS), diametral tensile strength (DTS), 4-point bending strength (BS) and degree of conversion (sum of brushite and monetite content in wt %) of cement samples printed with 20 % H<sub>3</sub>PO<sub>4</sub> after additional hardening in 20 % H<sub>3</sub>PO<sub>4</sub> for 3 × 60 s.

Sample	CS [MPa]	DTS [MPa]	BS [MPa]	Conversion [%]
printed with 20% H <sub>3</sub> PO <sub>4</sub>	5.3 ± 0.6	1.8 ± 0.1	2.1 ± 0.3	30
3 × 60s hardened in H <sub>3</sub> PO <sub>4</sub>	22.3 ± 1.5	3.2 ± 0.3	5.3 ± 0.6	67

At the same time, the tensile strength (bending strength) increased from approximately 1.8 MPa (2.1 MPa) to more than 3 MPa (5.3 MPa) combined with a higher degree of conversion to brushite of 67 % compared to 30 % for untreated samples. The increase in strength during storage in diluted phosphoric acid is accompanied by a decrease of porosity and average pore diameter from 45.5 % and 26.6 μm of untreated samples to 29.2 % and 12.5 μm for samples subsequently exposed to H<sub>3</sub>PO<sub>4</sub>, respectively, whereas the specific surface area characterized by the BET method increased from 2.3 to 4.0 m<sup>2</sup> g<sup>-1</sup> during post-hardening (Table 4). Figure 3 shows SEM micrographs of the porous structure of H<sub>3</sub>PO<sub>4</sub> treated sample and, at a higher magnification, the tabular brushite crystals that constituted the cement matrix microstructure were apparent.

Mechanical properties of cement samples printed with 10 % H<sub>3</sub>PO<sub>4</sub> before and after hydrothermal reaction at 134 °C (steam sterilisation) are shown in Table 5. This procedure leads to a full conversion of brushite to the anhydrite monetite in conjunction with a decrease of the mechanical performance and an increase of porosity.

**Table 4.** Average pore diameter, porosity determined using mercury porosimetry and specific surface area of samples printed with 20 % H<sub>3</sub>PO<sub>4</sub> and hardened for 3 × 60 s in 20 % H<sub>3</sub>PO<sub>4</sub>.

Sample	Average pore diameter [μm]	Porosity [%]	Specific surface area [m <sup>2</sup> g <sup>-1</sup> ]
printed with 20% H <sub>3</sub> PO <sub>4</sub>	26.6	45.5	2.3
printed with 20% H <sub>3</sub> PO <sub>4</sub> and post hardened for 3 × 60s in 20% H <sub>3</sub> PO <sub>4</sub>	12.5	29.3	4.0

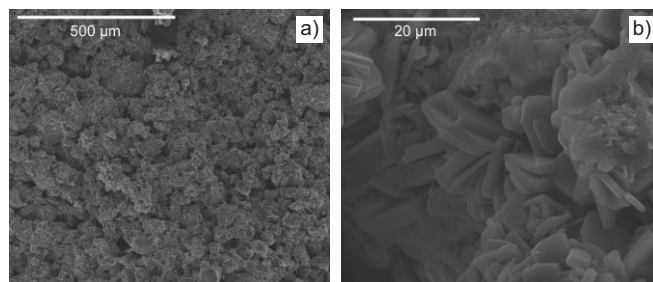


**Figure 3.** Microstructures of printed brushite/TCP matrices with 20 % H<sub>3</sub>PO<sub>4</sub> (left) after subsequent exposure to 20 % H<sub>3</sub>PO<sub>4</sub> (3 × 60 s) (right).

**Table 5.** Influence of hydrothermal treatment (134 °C, 2 h) on the compressive strength (CS), diametral tensile strength (DTS), porosity and phase composition of calcium phosphate materials. Samples (12 × 6 mm<sup>2</sup>) were printed with 10 % H<sub>3</sub>PO<sub>4</sub> following 3 × 30 s post-hardening in 20 % phosphoric acid.

Property	Brushite	Monetite
CS [MPa]	23.4 ± 3.3	15.3 ± 1.1
DTS [MPa]	3.3 ± 1.2	2.7 ± 0.3
Porosity [%]	38.8	43.8
Phase composition	51% Brushite, 12% Monetite, 26% β-TCP, 11% α-TCP	63% Monetite, 26% β-TCP, 11% α-TCP

In order to monitor printed implant degradation without animal sacrifice, X-ray micrographs of implanted CaP structures (brushite and monetite) were recorded 8, 32, and 56 weeks post implantation (Fig. 4). It was clearly apparent that dissolution of monetite cylinder seemed to be faster than for the brushite cylinder, which can be seen by a stronger decrease of both the implant projection area and the grey scale of the brushite implants in the X-ray micrographs as indicated in

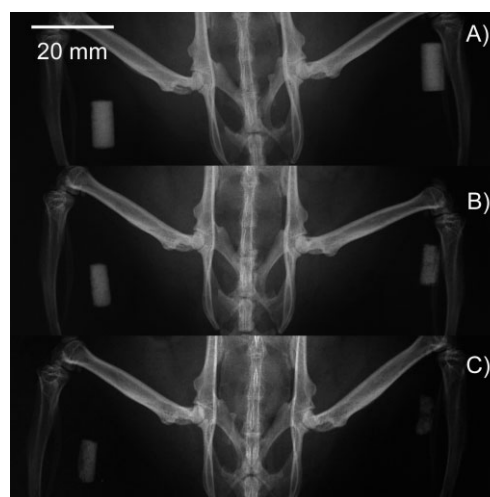


**Figure 4.** X-ray micrographs showing powder printed calcium phosphate samples after intramuscular implantation for A) 8 weeks, B) 32 weeks, and C) 56 weeks; left side: brushite structures, right side: monetite structures obtained by hydrothermal conversion of the brushite matrix.

Table 6. X-ray diffraction analysis (Table 7) of retrieved implants after 4 weeks implantation confirmed the faster degradation of the secondary phosphates brushite and monetite compared to the TCP phase, in case of the brushite implants, approximately 18 wt % hydroxyapatite was formed within the implant after 4 weeks.

**Table 6.** Results of image analysis of the X-ray micrographs in Figure 4. For each time point, the medium grey scale of each implant as well as the projection area (in pixels) was determined using Adobe Photoshop 7.0 software.

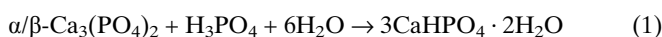
Implantation time [weeks]	Medium grey scale [%]		Implant projection area [Pixels]	
	Brushite	Monetite	Brushite	Monetite
8	73 ± 20	66 ± 18	11671	11965
32	59 ± 16	42 ± 14	9038	8650
56	35 ± 11	19 ± 5	7363	4683

**Table 7.** Phase composition according to Rietveld refinement analysis of explanted calcium phosphate samples; brushite samples were printed with 20 % H<sub>3</sub>PO<sub>4</sub> following 1 × 60 s post-hardening in 20 % H<sub>3</sub>PO<sub>4</sub>, monetite samples were obtained by autoclaving the brushite implants at 134 °C for 2 h

Sample	Brushite [wt %]	Monetite [wt %]	β-TCP [wt %]	α-TCP [wt %]	HA [wt %]
Brushite, pre-implantation	51	12	26	11	–
Monetite, pre-implantation	–	62	26	12	–
Brushite 4 weeks	26	13	30	13	18
Monetite 4 weeks	–	55	30	15	–

### 3. Discussion

3D powder printing is an attractive technology due to its potential to rapidly produce 3D geometries. The printing technique is commonly performed with gypsum or starch materials and an aqueous binder system (which are infiltrated with epoxy polymer after printing for reinforcement) and used for rapid prototyping in technical applications. In various studies the 3D printing method was extended to other powder/liquid printing systems, e.g., zinc oxide/acrylate cements.<sup>[18]</sup> In this study we combined calcium phosphate cement chemistry and 3D powder printing technique. The hardening of the samples during printing occurred via an acid base reaction between the α/β-TCP powder and the phosphoric acid binder phase, which rapidly forms brushite according to Equation 1:



Suitable TCP powders were produced in this study by sintering of a CaHPO<sub>4</sub>/CaCO<sub>3</sub> powder mixture at 1400 °C. This powder enabled printing of complex 3D structures (Fig. 1) with a dimensional accuracy of ± 200 μm. The deviation of the obtained dimension was nearly isotropic and less than 5 % differ-

ent from the theoretical value, which might be a result of a small expansion of the cement matrix during setting. The printed structures consisted of a brushite binder phase (up to 67 wt %) and remaining α/β-TCP phase and were shown to have a nearly homogeneous composition as evidenced by measuring the Ca/P ratio on a cross-sectional area of a 10 × 20 mm<sup>2</sup> cylinder using EDX analysis. The results showed a Ca/P ratio of 1.09 ± 0.08 at the outside, 1.02 ± 0.08 in the centre, and 1.05 ± 0.20 at half of the distance between the outside and the centre.

Printed bioceramics are of interest for both direct bone substitutes in low load-bearing areas, e.g., craniofacial, as well as scaffolds for tissue engineering applications. An adequate resistance to external load is one criterion if the printed structures shall be used as bone replacement material, even if the main functional application is not load bearing but to act as a support for the surrounding soft tissue. Factors influencing strength of printed samples were the acid concentration used for printing, which led to both a higher degree of conversion to brushite and a higher density and lower porosity of the matrix, respectively. Both factors are well known to affect the mechanical performance of calcium phosphate materials, e.g., a linear relation of cement strength with the degree of conversion in cement matrices has been reported<sup>[19]</sup> and an exponential relationship between the compressive strength of cement materials and their porosity is well known.<sup>[20]</sup> Strengths found in this study were up to 22 MPa under compressive load, which are higher than those commonly obtained for brushite cement mixtures based on TCP or HA/phosphoric acid solutions. Barralet et al.<sup>[21]</sup> found an ultimate compressive strength of brushite cement formed from nanocrystalline hydroxyapatite and diluted phosphoric acid (2 mol l<sup>-1</sup> and 3 mol l<sup>-1</sup>) of approximately 5–8 MPa after wet setting for 24 h. The reason for this behaviour is obviously the higher porosity if cements are formed with phosphoric acids. Due to the high reactivity and rapid hardening of these pastes, low powder to liquid ratios have to be used to obtain kneadable pastes. In contrast, a fast setting reaction with relatively high phosphoric acid concentrations is advantageous for printing since it leads to a rapid hardening of the structures. The plate-like microstructure of matrices mainly consisting of brushite crystals might also be responsible for an additional increase in strength, because crack deflection processes can be initiated, and thus lowering the effective fracture energy during mechanical load.

Due to their chemical composition consisting of up to 67 % brushite and unreacted tricalcium phosphate, these materials are expected to be resorbable *in vivo*. The solubility constants  $K_s$  of brushite ( $K_s = 2.57 \times 10^{-7} \text{ mol}^2 \text{ l}^{-2}$ ) and β-TCP ( $K_s = 3.16 \times 10^{-26} \text{ mol}^5 \text{ l}^{-5}$ ) are much higher compared to hydroxyapatite ( $K_s = 1.58 \times 10^{-117} \text{ mol}^{18} \text{ l}^{-18}$ ) at 25 °C,<sup>[2]</sup> respectively, such that a volume resorption of brushite and TCP can occur by simple chemical dissolution under physiological conditions. This resorption ability of brushite bone substitutes has previously been shown by various groups *in vitro*<sup>[22,23]</sup> and *in vivo*.<sup>[24–26]</sup> In contrast, degradation of apatitic substitutes is only possible by acid producing bone remodeling cells and is limited to surface degradation since osteoclasts cannot penetrate the



microporous cement. In this case macropores have to be introduced into the structure to enable degradation *in vivo*.<sup>[27–29]</sup>

The degradation ability was confirmed in this study *in vivo* following intramuscular implantation in rats. Implantation in muscles was performed for two reasons. Firstly, resorption studies in bone have the disadvantage that it is impossible to distinguish between a chemical degradation due to the differences in solubility of calcium phosphates and cellular mediated degradation via osteoclasts. Secondly, intramuscular implantation allows degradation analysis by using X-ray micrographs without sacrificing the animals. Since the materials in this study have very similar radio-opacity to bone, these measurements are not possible in living animals if orthotopic implantation is preferred. In order to perform intramuscular implantation we were limited to cylindrical geometries to avoid tissue irritation at sharp corners. While a cylindrical geometry was neither technically demanding nor a good demonstration model for our capacity to control shape and macroporosity,<sup>[30]</sup> it enabled us to have only one external surface available for ion exchange and the implantation of a simple defined geometry enabled us to quantify dissolution from X-ray analyses.

Two different matrices were tested *in vivo*: firstly brushite as printed and secondly monetite which was obtained by hydrothermal dehydration of the brushite matrix. Since monetite has a higher density than brushite (2.89 g cm<sup>-3</sup> compared to 2.3 g cm<sup>-3</sup>), this results in an increase of porosity from 38 % to 43 % and a slight decrease in strength (Table 5). Surprisingly, the monetite structures were dissolved faster than the brushite samples although the latter is chemically more soluble, the solubility constants found in literature<sup>[2,31]</sup> are reported to be  $K_s = 2.57 \times 10^{-7} \text{ mol}^2 \text{ l}^{-2}$  for brushite and  $K_s = 1.25 \times 10^{-7} \text{ mol}^2 \text{ l}^{-2}$  for monetite. The reason for the higher degradation rate of monetite is thought to be related to changes of the phase composition of the materials *in vivo*. For both matrices, the secondary phosphates monetite and brushite are dissolving (faster than the tricalcium phosphate phases), however differences occur for the brushite structure where initially hydroxyapatite is formed by a dissolution/precipitation reaction. This insoluble HA retards *in vivo* degradation. A similar behavior was found for brushite forming cements by other groups.<sup>[25,32]</sup> It has been reported that *in vivo* HA formation in brushite cements can be suppressed for example by adding magnesium<sup>[33]</sup> or pyrophosphate<sup>[34]</sup> ions to the matrix which act as strong inhibitors of hydroxyapatite crystal growth.

## 4. Conclusion

3D powder printing of tricalcium phosphate with diluted phosphoric acid as binder enabled the fabrication of custom made brushite/TCP implants with well defined architecture and the ability of being resorbed *in vivo*. If long term stable implants would be clinically required, the brushite matrix has to be converted to less soluble apatite, preferably by a hydrothermal conversion process as described recently for brushite coatings on titanium alloys.<sup>[35]</sup>

## 5. Experimental

TCP was synthesized by heating a mixture of dicalcium phosphate anhydrous (DCPA, CaHPO<sub>4</sub>, monetite) (Merck, Darmstadt, Germany) and calcium carbonate (CC, CaCO<sub>3</sub>, calcite) (Merck, Darmstadt, Germany) in a 2:1 molar ratio to 1400 °C for 7 h followed by quenching to room temperature. The sintered cake was crushed with a pestle and mortar and passed through a 160 µm sieve. Subsequent milling of TCP was performed in a planetary ball mill (PM400, Retsch, Germany) for 10 min.

Printing of cement samples was performed with a 3D-powder printing system (Z-Corporation, USA) using the TCP powder and diluted phosphoric acid (H<sub>3</sub>PO<sub>4</sub>) (Merck, Darmstadt, Germany) with concentrations of 5, 10, 20, 30, and 40 wt %, respectively. Approximately 9 kg of TCP powder were filled into the printer and manually compressed using a metal plate. The powder bed for the printed samples was prepared in the same way using 1 kg TCP powder. Sample geometries like cylinders, rings, and cuboids were obtained using CAD software or directly taken from CT scan data for printing irregular bone structures. Printing parameters used were: a layer thickness of 100 µm, and an isotropic scaling  $x = y = z = 1.0$ .

Compressive strength testing was performed with cylindrical samples with a height of 20 mm and a diameter of 10 mm under axial compression at a crosshead speed of 1 mm/min using a static mechanical testing device (Zwick 1440, Ulm, Germany) and a 5 kN load cell. Prior to testing, the minimum and maximum diameter and the height of the samples were measured to estimate the dimensional accuracy of the printing process. Samples for diametral tensile strength (DTS) testing ( $h = 5 \text{ mm}$ ,  $d = 10 \text{ mm}$ ) and those for testing the 4-point bending strength (cuboids with  $h = 10 \text{ mm}$ ,  $b = 5 \text{ mm}$ ,  $l = 80 \text{ mm}$ ) were tested with a cross-head speed of 10 mm min<sup>-1</sup>. The DTS was calculated from:

$$\text{DTS (MPa)} = 2F_{\text{max}}/(\pi * d * h) \quad (1)$$

where  $d$  = diameter (10 mm),  $h$  = height of the sample (5 mm) and  $F_{\text{max}}$  is the failure load. The bending strength was calculated according to:

$$\text{BS (MPa)} = 3F_{\text{max}} * (L_1 - L_2)/(b * h^2) \quad (2)$$

where  $F_{\text{max}}$  is the failure load,  $L_1$  ( $L_2$ ) is the distance between the outer (inner) rolls,  $b$  = width and  $h$  = height of the samples. Testing of all samples was performed after storage in air at room temperature for 24 h. The samples printed with 20 % H<sub>3</sub>PO<sub>4</sub> were additionally stored in the same solution for 3 x 60 s followed by 1 h storage in air prior to testing to obtain a higher degree of conversion to brushite. The porosity of the samples was calculated from the apparent density after drying and the true density calculated from the phase composition using literature density values [31]. Porosity and pore size distribution were measured by high pressure Hg-porosimetry (Porosimeter 2000, Carlo Erba Instr., Milano, Italy). The Brunauer Emmet Teller method (BET) was used to determine the specific surface area within the porous calcium phosphate matrices (Micromeritics, ASAP 2000, USA). The microstructure of fracture surfaces was characterized by scanning electron microscopy (SEM) (FEI, Quanta 200, Czech Republic). The homogeneity of the materials was determined using EDX analysis (INCA x-sight, Oxford Analytical Instruments, Abington, UK) on a cross-sectional area of a 10 x 20 mm<sup>2</sup> cylinder, which was 3x60s post-hardened in 20 % H<sub>3</sub>PO<sub>4</sub> and thermally converted to monetite at 150 °C h<sup>-1</sup>. Four measurements, respectively, were taken at the outside, the centre and at half of the distance between the outside and the centre to determine the Ca/P ratio.

X-ray diffraction (XRD) patterns of set cements were recorded using monochromated Cu K<sub>α</sub> radiation (D5005, Siemens, Karlsruhe, Germany). Data were collected from  $2\theta = 20\text{--}40^\circ$  with a step size of  $0.02^\circ$  and a normalized count time of 1 s/step. The phase composition was checked by means of JCPDS reference patterns for  $\alpha$ -TCP (PDF Ref. 09-0348),  $\beta$ -TCP (PDF Ref. 09-0169), monetite (PDF Ref. 09-0080) and brushite (PDF Ref. 09-0077). Quantitative phase relations of the

composite materials were calculated by means of total Rietveld refinement analysis using the TOPAS software (Bruker AXS, Karlsruhe, Germany). As references the system internal database structures of  $\alpha$ -TCP,  $\beta$ -TCP, brushite and monetite were used together with a Chebyshev fourth order background model and a Cu K $\alpha$  emission profile.

Implantation experiments were performed intramuscular in Sprague-Dawley rats ( $n = 12$ ) with a medium age of 6 months and an average weight of approx. 450 g. Experiments were approved by the local Ethical Committee and veterinary authorities (No. 621-2531.01-11/05). Cylindrical implants ( $d = 5$  mm,  $h = 10$  mm) were printed with 20 %  $H_3PO_4$  following 3 x 30 s post-hardening in 20 %  $H_3PO_4$ . Two different matrices were implanted: (1) implants predominately composed of brushite as obtained after printing, these implants were sterilised by soaking in 70 % ethanol over night following drying under sterile conditions in a laminar flow chamber and (2) implants predominately composed of monetite which were obtained after autoclaving the brushite implants at 134 °C for 2 h. Both types were implanted into the femoral extensor muscles of each animal (one left, one right) after intraperitoneal anaesthetic with a mixture of Ketavet (120 mg/kg weight) and Rompun (5 mg/kg weight). Radiographic control of the implants was performed every 4 weeks. The X-ray micrographs were analysed by determining the medium grey scale of each implant as well as the implant projection area using Adobe Photoshop 7.0 software. Two animals were sacrificed after 4 weeks post implantation and the explanted matrices were examined due to changes of their phase composition using X-ray diffraction analysis.

Received: January 5, 2007

Revised: July 4, 2007

Published online: November 28, 2007

- [1] K. A. Gross, C. C. Berndt, *Rev. Mineral. Geochem.* **2002**, 48, 631.
- [2] M. Epple, S. V. Dorozhkin, *Angew. Chem. Int. Ed.* **2002**, 41, 3130.
- [3] R. Z. LeGeros, *Clin. Orthop.* **2002**, 39, 81.
- [4] M. Bohner, U. Gbureck, J. E. Barralet, *Biomaterials* **2005**, 26, 6423.
- [5] M. Bohner, *Injury* **2000**, 31 (Suppl. 4), D37.
- [6] K. A. Hing, *Int. J. Appl. Ceram. Technol.* **2005**, 2, 184.
- [7] Z. Sadeghian, J. G. Heinrich, F. Moztaradeh, *CFI Ceram. Forum Int.* **2004**, 81, E39.
- [8] C. E. Wilson, J. D. de Bruijn, C. A. van Blitterswijk, A. J. Verbout, W. J. A. Dhert, *J. Biomed. Mater. Res., Part A* **2004**, 68, 123.
- [9] N. K. Vail, L. D. Swain, W. C. Fox, T. B. Aufdemorte, G. Lee, J. W. Barlow, *Mater. Des.* **1999**, 20, 123.
- [10] K. H. Tan, C. K. Chua, K. F. Leong, C. M. Cheah, P. Cheang, M. S. Abu Bakar, S. W. Cha, *Biomaterials* **2003**, 24(18), 3115.
- [11] C. K. Chua, K. F. Leong, K. H. Tan, F. E. Wiria, C. M. Cheah, *J. Mater. Sci. Mater. Med.* **2004**, 15, 1113.
- [12] S. H. Irsen, B. Leukers, C. Höckling, C. Tille, H. Seitz, *Materialwiss. Werkstofftech.* **2006**, 37, 533.
- [13] B. Leukers, H. Gulkan, S. H. Irsen, S. Milz, C. Tille, M. Schieker, H. Seitz, *J. Mater. Sci. Mater. Med.* **2005**, 16, 1121.
- [14] H. Seitz, W. Rieder, S. Irsen, B. Leukers, C. Tille, *J. Biomed. Mater. Res. Part B* **2005**, 74, 782.
- [15] L. Xiang, D. C. Li, B. H. Lu, Y. P. Tang, L. Wang, Z. Wang, *Rapid Prototyping J.* **2005**, 11, 312.
- [16] H. Eufinger, C. Rasche, J. Lehmbruck, M. Wehmöller, S. Weihe, I. Schmitz, C. Schiller, M. Epple, *Biomaterials* **2007**, 28, 475.
- [17] M. Bohner, P. vanLanduyt, H. P. Merkle, J. Lemaître, *J. Mater. Sci. Mater. Med.* **1997**, 8, 675.
- [18] A. Pfister, U. Walz, A. Laib, R. Mulhaupt, *Macromol. Mater. Eng.* **2005**, 290, 99.
- [19] U. Gbureck, O. Grolms, L. M. Grover, J. E. Barralet, R. Thull, *Biomaterials* **2003**, 24, 4123.
- [20] J. E. Barralet, M. Hofmann, L. M. Grover, U. Gbureck, *Adv. Mater.* **2003**, 15, 2091.
- [21] J. E. Barralet, K. J. Lilley, D. F. Farrar, C. Ansell, U. Gbureck, *J. Mater. Sci. Mater. Med.* **2004**, 15, 405.
- [22] L. M. Grover, J. C. Knowles, G. J. P. Fleming, J. E. Barralet, *Biomaterials* **2003**, 24, 4133.
- [23] L. M. Grover, U. Gbureck, A. J. Wright, M. Tremayne, J. E. Barralet, *Biomaterials* **2006**, 27, 2178.
- [24] F. Theiss, D. Apelt, B. A. Brand, A. Kutter, K. Zlinszky, M. Bohner, S. Matter, C. Frei, J. A. Auer, B. von Rechenberg, *Biomaterials* **2005**, 26, 4383.
- [25] B. Flautre, C. Delecourt, M. C. Blary, P. Van Landuyt, J. Lemaître, P. Hardouin, *Bone* **1999**, 2, 35S.
- [26] J. M. Kuemmerle, A. Oberle, C. Oechslin, M. Bohner, C. Frei, I. Boecken, B. von Rechenberg, *J. Cranio-Maxill. Surg.* **2005**, 33, 37.
- [27] H. H. K. Xu, S. Takagi, J. B. Quinn, L. C. Chow, *J. Biomed. Mater. Res., Part A* **2004**, 68, 725.
- [28] M. C. von Doernberg, B. von Rechenberg, M. Bohner, S. Grunfelder, G. H. van Lenthe, R. Muller, B. Gasser, R. Mathys, G. Baroud, J. Auer, *Biomaterials* **2006**, 27, 5186.
- [29] J. E. Barralet, L. M. Grover, T. Gaunt, A. J. Wright, I. R. Gibson, *Biomaterials* **2002**, 23, 3063.
- [30] U. Gbureck, T. Hölzel, C. Doillion, F. A. Müller, J. E. Barralet, *Adv. Mater.* **2007**, 19, 795.
- [31] J. C. Elliott, *Structure and Chemistry of the Apatites and Other Calcium Orthophosphates*, Elsevier, Amsterdam **1994**.
- [32] B. R. Constantz, B. M. Barr, I. C. Ison, M. T. Fulmer, J. Baker, L. McKinney, *J. Biomed. Mater. Res.* **1998**, 43, 451.
- [33] S. Rousseau, J. Lemaître, M. Bohner, C. Frei, presented at GRIBOI 2002, ##Shanghai, China, March 14–17, **2002**.
- [34] L. M. Grover, U. Gbureck, A. J. Wright, J. E. Barralet, *J. Am. Ceram. Soc.* **2005**, 88, 3096.
- [35] Y. Han, K. W. Xu, J. A. Lu, *J. Mater. Sci. Mater. Med.* **1999**, 10, 243.